Article in Press

Universal framework for efficient estimation of stability in multi-principal element alloys

Lin Wang, Bo Shen, Zheng-Da He, Zihao Ye, Yan Zeng, Chad A. Mirkin & Bin Ouyang

We are providing an unedited version of this manuscript to give early access to its findings. Before final publication, the manuscript will undergo further editing. Please note there may be errors present which affect the content, and all legal disclaimers apply.

If this paper is publishing under a Transparent Peer Review model then Peer Review reports will publish with the final article.

Universal Framework for Efficient Estimation of Stability in Multi-Principal Element Alloys

Lin Wang[1]†, Bo Shen[2,3]†, Zheng-Da He[1], Zihao Ye[2,3], Yan Zeng[1], Chad Mirkin[2,3], Bin Ouyang[1,*]

[1]Department of Chemistry and Biochemistry, Florida State University, Tallahassee, FL 32304, USA.

[2]Department of Chemistry, Northwestern University, Evanston, Illinois 60208, USA.

[3]International Institute for Nanotechnology, Northwestern University, Evanston, Illinois 60208, USA.

†These authors contributed equally to this work
*To whom correspondence may be addressed. E-mail: bouyang@fsu.edu

Abstract

Predicting the synthetic accessibility of multi-principal element alloys (MPEAs) across the global chemical space remains a challenge. In this study, we show that the synthesizability of MPEAs across broad compositional and structural spaces can be predicted using a physical model that expresses the total energy of any MPEA as a linear combination of energies from lower-dimensional subsystems. The model is validated with a large computational dataset and supported by the experimental synthesis of multiple MPEAs, achieving mean absolute errors near or below 7 meV/atom on a density functional theory dataset of 135,791 MPEAs spanning 28 metals and up to ten components. Its accuracy is comparable to state-of-the-art deep learning models while maintaining interpretability through cluster-expansion theory. Moreover, we show that the stability of high-entropy alloys can be predicted using a linear combination of energies from lower-dimensional systems with low errors, indicating a flatter energy landscape at high compositional complexity.
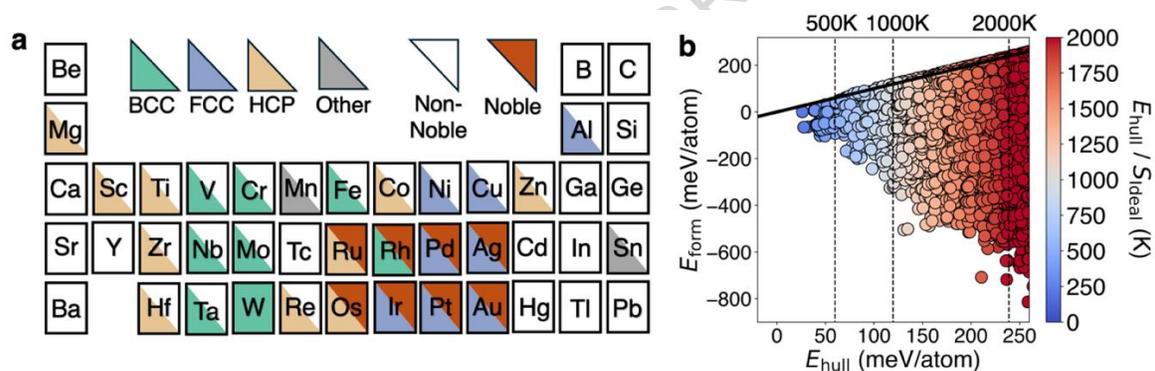
Introduction

Multi-principal element alloys (MPEAs) [1-12], including medium- and high-entropy alloys, have emerged as promising materials in various fields due to their extensive compositional space and potential for diverse applications [9-19]. However, predicting the synthesizability of MPEAs remains a challenge, which has slowed down the synthesis explorations. Earlier work examined HEA formation using binary formation energies as an initial screening approach [20]. Subsequent studies have explored a variety of approaches using machine learning (ML) models and heuristic theories [3,21-26]. However, these models often struggle with limited accuracy and/or interpretability [27,28]. Despite notable progress in predicting synthesizability of MPEA [3,21-26] and high entropy materials [29,30], interpretable physical models for predicting phase stability across global chemical space of MPEAs remain lacking. Three key questions persist: 1) Is there a universal rule governing MPEA stability? 2) What is the crucial data to reveal MPEA stability across different compositions and dimensionality? and 3) What factors limit the accuracy of phase stability predictions for MPEAs?

In this work, we address the above questions by combining theoretical and experimental approaches. We present a physical model that can serve as universal model for predicting the synthesizability of MPEA with any composition and dimensionality. This model is validated on a dataset of 135,791 density functional theory (DFT)-computed MPEA structures covering 28 typical metals, showing a mean absolute error (MAE) as low as 6.956 meV/atom for predicting synthesizability of MPEAs. Such performance matches the state-of-the-art graph neural network models [31] trained on the same dataset [32]. The reliability of our computational dataset and stability metric can be supported by successful synthesis of nine previous unreported MPEAs and accurate prediction of 30 out of 32 experimentally reported MPEAs synthesized below 1273K. It also supports the stability rule for MPEAs: the energy and hence stability of a high-dimensional MPEA

can be reasonably approximated by a weighted combination of the energies of its lower-dimensional constituent subsystems. More importantly, we uncover two unprecedented phenomena: 1) accurate determination of the synthesizability of any MPEA compositional space can be achieved with small datasets; Specifically, when focusing on a subset of MPEA including N metals, as few as C_N^3 DFT calculations are sufficient to predict the energy of all corresponding MPEAs; and 2) there is a decaying of decomposition energies of higher dimensional MPEA to lower dimensional MPEA with the trend being more pronounced when dimensionality goes up.

Results

Formation energy and energy above hull

Fig. 1. Chemical space and data distribution of the MPEA dataset. a, The bottom left triangle represents the room temperature phases as elemental metal of selected metal, Mn and Sn marked as "other" because the room temperature phases are none of the three phases (BCC/FCC/HCP). The top-right triangle distinguishes each metal as either a noble or a non-noble metal; **b**, Scatter plot of formation energy (E_{form}) and energy above hull (E_{hull}) for all 4M MPEAs that can be entropically stabilized below 2000 K (the stabilization temperature is calculated from $E_{\text{hull}}/S_{\text{ideal}}$. Here, S_{ideal} is the ideal mixing entropy, defined as $S_{\text{ideal}} = k_B ln(n_{\text{M}})$ with k_B as the Boltzmann constant and n_{M} as the number of metal elements in MPEA). Blue and red represent low and high temperatures, respectively. The solid black line represents the line $E_{\text{form}} = E_{\text{hull}}$. Three dashed lines represent the maximum E_{hull} values of 4M MPEAs that can be stabilized at 500 K, 1000 K, and 2000 K, respectively, assuming ideal mixing entropy.

We create a comprehensive database to investigate the stability of MPEAs with increasing compositional complexity. This database includes MPEAs with two, three, four, and five equimolar compositions (denoted as 2M, 3M, 4M, and 5M) from 28 metals (8 noble metals and 20 non-noble metals, Fig. 1a). The 2M, 3M, and 4M MPEAs were generated by enumerating across
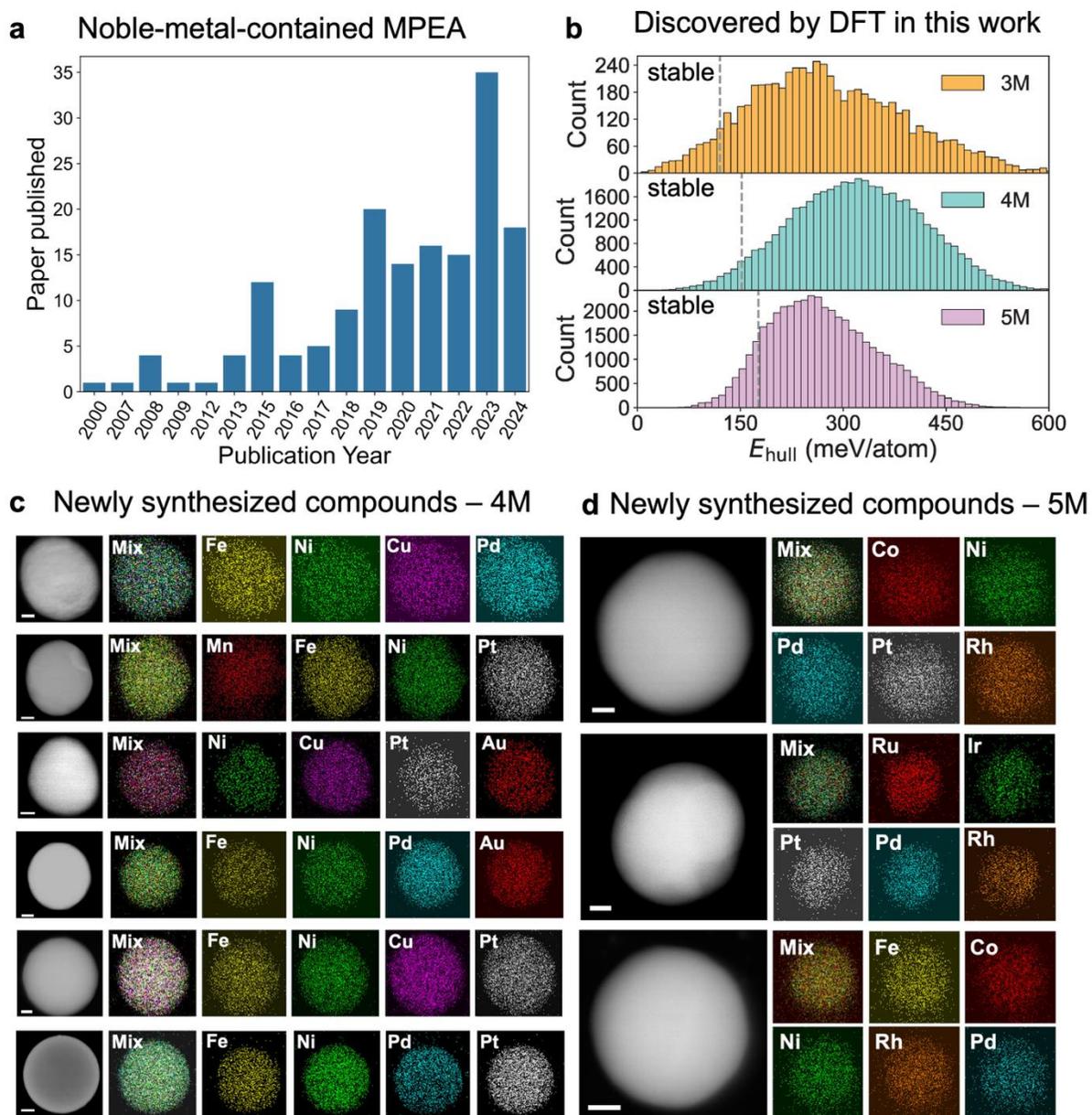
this 28-metal space, yielding 24,129 ($= C_{28}^2 + C_{28}^3 + C_{28}^4$) MPEAs with distinct compositions. We also enumerate all combinatorial space among quaternary equimolar MPEAs that can be entropy-stabilized below 1273 K with the leftover 24 metals, which yielded another 18,014 equimolar MPEAs compositions with five metal elements. For each composition, three different crystal structures, FCC, HCP, and BCC, are initialized for DFT calculations, resulting in a total of 126,429 DFT-optimized MPEA structures.

The stability of MPEAs is commonly characterized by two quantities: formation energy (E_{form}) and energy above hull (E_{hull}). The value E_{form} is defined as the energy released when forming an MPEA from pure elemental phases and E_{hull} is a generalized measure of stability that assesses the largest driving force for an MPEA to decompose into any potential ground state (metal or intermetallic) in its high-dimensional phase diagram [33-35]. We establish the E_{hull} values by constructing phase diagrams that include all experimentally reported metals and intermetallic phases, as well as all hypothetical low-energy structures hosted in both Materials Project [36] and the Open Quantum Materials Database (OQMD) [37,38]. This approach results in a competing phase pool containing 6,723 metals and intermetallic phases. Particularly, 53, 754, and 11,996 quaternary MPEAs are capable of being stabilized below 500 K, 1000 K, and 2000 K, respectively (Fig. 1b). Both E_{form} and E_{hull} present in Fig. 1b are calculated at 0 K, with the black line ($E_{form} = E_{hull}$) indicating cases where decomposition leads to elemental phases. Structural-dependent plots are shown in Supplementary Figure 1; the energy distributions across FCC, BCC, and HCP structures are similar, and a summary of the number of 4-metal MPEAs stabilized under different temperatures and phases is provided in Supplementary Figure 2. To examine the correlation between the two stability descriptors and commonly used physical parameters, we adopt the same plotting style as in Fig. 1b, coloring the data points by valence electron concentration (VEC),

average electronegativity (χ_{ave}), and average off-lattice displacement (ε_{ave}) (see Supplementary Figure 3). These analyses reveal no clear or systematic trends, although compositions with large off-lattice displacements generally correspond to instability. These observations further highlight the complexity of stability prediction in high-entropy systems, emphasizing the need for models that are both predictive and physically interpretable.

Experimental validation of predicted MPEAs

Among all MPEA compositions, noble-metal-containing MPEAs emerge as a distinct and underexplored group in terms of compositional coverage. As shown in Fig. 2a, this compositional space remains relatively underexplored, with only about one hundred reported compositions published[39-46] from our survey (Supplementary Figure 4 and Supplementary Table 1), in contrast to over several thousand papers and compositions reported for other MPEAs [4,47]. Furthermore, the ease of reducing noble-metal precursors in a hydrogen atmosphere facilitates their synthesis using techniques such as scanning probe block copolymer lithography. Notably, Noble-metal-containing MPEAs have also garnered significant attention due to their great potential in catalysis and other applications[1,16,17,39,40,48]. Therefore, our experimental validation efforts will primarily focus on noble-metal-containing MPEAs. In this work, using high-throughput phase diagram calculations, we find 647 ternary, 2,178 quaternary, and 5,478 quinary noble-metal-containing MPEAs that can be stabilized below 1273 K with ideal mixing entropy (Fig. 2b).

Fig. 2. Previously reported noble metal-containing MPEAs and non-reported MPEAs discovered in this work. a, Number of papers published on noble-metal-containing MPEAs from 2000 to 2024. (Counts are derived from papers listed in the Supplementary References). **b**, Histogram of the energy above hull of the noble-metal-containing 3-5M MPEAs investigated in this work. The dashed lines represent where the entropy-stabilization temperature is less than 1273 K. **c**, STEM images and EDX elemental mappings of six synthesized noble-metal-containing 4M MPEAs with different compositions. **d**, STEM images and EDX elemental mappings of three synthesized noble-metal-containing 5M MPEAs with different compositions. Scale bars = 10 nm.

To verify the reliability of using E_{hull} values as a stability descriptor, we select six quaternary

and three quinary MPEAs with stable temperatures below 1273K for synthesis (e.g., $E_{hull} <$

$S_{ideal} \times 1273K$). The compounds are: FeNiCuPd, MnFeNiPt, NiCuPtAu, FeNiPdAu, FeNiCuPt, FeNiPdPt, CoNiPdPtRh, RuIrPtPdRh, and FeCoNiRhPd (Supplementary Table 2, and E_{hull}, E_{form} value shown in Supplementary Figure 5). Example of how synthesizability is evaluated can be found in Supplementary Note 1. These nine MPEAs are carefully selected based on synthesis feasibility and theoretical predictions. We focus on noble-metal-rich compositions due to their enhanced reducibility under H_2, excluding early transition metals (e.g., Ti, V, Cr), other active metals such as Mg and Al, and toxic or volatile elements (e.g., Os, Zn, Sn) for safety and experimental limitations. Selection prioritized alloys with low predicted stabilization temperatures, high noble metal content, and compositions that are never reported before (with reported compounds listed in Supplementary Table 1). It should be noted that even though those materials are synthesized as nanoparticles. The size is controlled to be rather large (>50 nm) on purpose, which goes beyond the region of typical size-dependent phase stability, which usually limit to less than and close to 10 nm[49,50]. We thus consider the experiment to be comparable to our DFT calculations.

The MEPA nanoparticles (NPs) were prepared by scanning probe block copolymer lithography (SPBCL), a technique enabled by Dip Pen Nanolithography[51] and Polymer Pen Lithography[52]. (see Methods "Multimetallic nanoparticle (NP) synthesis") [53-57]. In this process, various metal precursors with equimolar ratio were dissolved in a block copolymer solution, which was then delivered by an atomic force microscope (AFM) tip to form polymer dome arrays on the substrate. After thermal annealing treatments, the metal precursors were reduced to form one NP in each dome (Supplementary Figure 6). In SPBCL, the amount of metal precursors in the polymer inks can be adjusted, allowing precise control of the chemical compositions of single NPs. More importantly, the SPBCL-prepared NPs can be heated at high temperatures (up to 1000 °C) without

particle aggregation, which is necessary to evaluate the thermal stabilities of MPEAs. The scanning transmission electron microscope (STEM) images and energy dispersive X-ray (EDX) elemental mappings of 4M (Fig. 2c) and 5M (Fig. 2d) MPEAs confirmed the successful synthesis of all predicted stable MPEAs with uniform element distribution and equal element concentrations (Supplementary Figure 7 and Supplementary Table 3). The experimental results validated that E_{hull} can be a useful metric to assess MPEA stability.

Elemental stability rules

In our established dataset of 126,429 DFT-computed MPEAs up to 5 metals, 8,303 MPEAs (6.56% of all compounds) with three to five elements are predicted to have stabilization temperatures below 1273 K. We consider these MPEAs as synthetically accessible MPEAs. A chord diagram (Fig. 3a), which charts the overall elemental compatibility between metals, was used to categorize the 28 metals considered in this study into noble metals (colored) and non-noble metals (gray). The thickness of each segment in the diagram is proportional to the occurrence (n_{stable}^{M}) of each metal (M) appearing in a stable MPEA that can be entropy stabilized below 1273K. The connections between segments indicate the occurrence ($n_{\text{stable}}^{M1-M2}$) when both metals (M1 and M2) coexist in an MPEA that can be entropy stabilized below 1273 K. The connections between non-noble metals are shown in Fig. 3c. Given the substantial enhancement in catalytic performance brought by the inclusion of noble metals, their impact is specifically emphasized in Fig. 3(b, d–k).

Fig. 3. Chord diagrams showing the pair-wise elemental stability of MPEAs. a, Pairs between all metals. b, Pairs between noble-noble metals. c, Pairs between non-noble metals. (d-k) Pair-wise connection for each noble metal (the same color is shown in a). Thickness is set in proportion to the probability of finding MPEA with given two metals with stabilization temperatures below 1273 K. Note that all chord diagrams from A to K have the same order of elements so that the small font size in D-K can be seen using A as a reference.

The elemental stability mapping in Fig. 3 provides insights into the compatibilities and preferences of metal species within MPEAs. Specifically, we find that Rh and Pt stand out as the most compatible noble metals (Fig. 3a, 3b, 3d and 3e), while Ni and Fe are the most compatible non-noble metals (Fig. 3a and 3c). In contrast, Ag and Au are the most selective noble metals when forming MPEAs (Fig. 3a, 3b, 3j and 3k). Sc, Hf, Zr, and Ta are found to form stable MPEAs with a limited range of other metals (Sc: 203, Hf: 370, Zr: 313, Ta: 553). In terms of elemental pairing preferences, Rh, Pt, and Ru generally show broad compatibility with most elements, as highlighted by the extensive pairing data (Rh: 3175, Pt: 2777, Ru: 2391). In comparison, stable MPEAs containing Ag are selectively formed, primarily with Au, Pt, Pd and Zn.

The observed trends align with general periodic table groupings and proximities; metals from the same group (e.g., Pd-Pt, Ru-Os, Ag-Au) or adjacent positions in a row (e.g., Ir-Pt, Ru-Rh, Rh-Pd) often exhibit higher pairing probabilities. These trends are supported by their close atomic properties, such as electronic structure and atomic radius, in accordance with the Hume-Rothery rules [58]. The latter group FCC metals, including noble metals such as Rh, Pt, Pd, and Ir, as well as non-noble metals such as Ni and Cu, present enhanced compatibility in MPEAs across different structures. This compatibility extends to Fe, Co, Mn, and Cr, aligning with the discovery of the Cantor alloy (CrMnFeCoNi) [59] and its various single-phase modifications [1,60-62].

The elemental stability rules we have uncovered provide insights into previously reported experimental efforts on MPEAs (detailed in Supplementary Figure 4 and Supplementary Table 1). The MPEAs containing Ru, Pd, Ag and Pt have been frequently investigated, aligning with our findings that noble-metal-containing MPEAs tend to be stable (6,928 of the 8,303 stable MPEAs contain noble metals). We can also link the high frequency of specific elemental pairs, such as Pd-Pt, Rh-Pt, and Rh-Pd reported in the literature, to their high probability (thick segment, Fig. 3b).

Prior research validating the stability of Ag-Zn in alloys supports our prediction [63,64]. In this work, the successful synthesis of nine MPEAs incorporating noble metals (Pt, Pd, and Au) with non-noble metals (Ni, Fe, Cu, Mn, and Cr) further verifies the reliability of the elemental stability rules.

Universal framework across extended dimensionalities and compositions

Beyond elemental compatibility, the stability of MPEAs is also influenced by their dimensionality - the number of distinct elements in a single-phase alloy. With growing interest in the synthesis and application of high-dimensional MPEAs, the challenge lies in the ability to predict their stability accurately and efficiently at extended dimensionality. Here, we demonstrate that a simple linear model can be used to effectively estimate the stability of MPEAs across various dimensionalities.

The core hypothesis of our model is that the total energy of an MPEA can be expressed as a linear summation of contributions from various atomic clusters. These clusters refer to local atomic arrangements present in the MPEA structure, defined in the same manner as in the typical cluster expansion theory [65]. The construction of total energy from energies of different local clusters has been widely used in cluster expansion theory [34,65-72], from simple alloys to high-entropy solid solutions. This concept can be expressed as:

$$E = \sum_i J_i n_i + \sum_{i,j} J_{ij} n_{ij} + \sum_{i,j,k} J_{ijk} n_{ijk} + \cdots \tag{1}$$

where J_i, J_{ij}, and J_{ijk} represent the energy contributions from singlets (single atom), pairs, and triplets, respectively, while n_i, n_{ij}, and n_{ijk} refer to the concentrations or counts of these clusters. This formalism has inspired the development of our model, which proposes that the total energy of higher-dimensional MPEAs can be approximated by summing the energies of lower-

dimensional MPEAs, thus closely matching the averaged cluster probability of the target MPEA. Specifically, the model can be expressed as:

$$E_N \approx \sum_{i \in \left(1, C_N^M\right)} \varepsilon^i E_M^i \tag{2}$$

where E_N and E_M represent the total energy of an MPEA with N and M elements, respectively, and ε^i is the weighting factor in the summation. To represent an N-element MPEA as a combination of its M-component subspaces, a convenient and physically meaningful choice is $\varepsilon^i = \frac{1}{C_N^M}$ (see Supplementary Note 2), where C_N^M is the binomial coefficient denoting the number of possible M-component combinations from an N-component system. The uniform choice of ε^i ensures that the energy contributed by the singlet term cancels exactly when averaging over all subspaces, thereby reducing the overall cluster probability difference. It also helps conserve the elemental concentration across the ensemble of subspaces, as our model focuses on equimolar compositions, which lie at the center of the composition space and maximize configurational entropy. Numerically, we can use special quasi-random (SQS) structures to serve as the basis of MPEAs, as the cluster probabilities will closely approach the random limit [73,74] defined by the algorithms used to generate these structures. Utilizing SQS structures allows us to quantify the cluster concentrations for each MPEA structure.

Fig. 4. Performance of our predictive model. a, The theoretically derived mean absolute error (MAE) of predicting energy contribution from selective cluster 4M-10M MPEA using 2M-9M MPEA as basis. J_0 is used to represent the unit of energy, with the physical meaning being the energy contribution of certain cluster, e.g., J_{ii}, J_{ij}, J_{ijk} respectively. **b**, The MAE for using DFT-computed total energy of 2M-9M MPEA to predict 4M-10M MPEAs as a contrast to the theoretical derivation. **c**, The comparison between our physical model with a crystal graph convolutional neural network (CGCNN). Each bar represents a single value, not a statistical distribution.

As a result of setting ε^i as $1/C_N^M$ while the energy of each MPEA taken from SQS structures, the probabilities of pairs, triplets, and higher-order clusters are closely aligned. The differences in cluster concentration can be calculated as:

$$\Delta n_{c_p^q} = \left(\frac{1}{N}\right)^p - \frac{C_{N-q}^{M-q}}{C_N^M}\left(\frac{1}{M}\right)^p \tag{3}$$

where $\Delta n_{c_p^q}$ represents the cluster concentration difference of a cluster with p sites and q species

when fitting M-dimensional MPEAs using N-dimensional MPEAs as a linear basis (full derivation

in Supplementary Note 3). Utilizing Equation (2), we can predict the energy of an MPEA of any

dimension using lower-dimensional MPEAs with the analytic difference of cluster concentration

determined by Equation (3). To show the quantitative trends, the analytic energy difference

contributed by self and cross terms of pair interactions can be represented by the top two panels of

Fig. 4a, while the energy difference contributed by cross term of triplet interactions can be

represented by the bottom panel in Fig. 4a. For all three clusters shown in Fig. 4a, the energy

difference decays and approaches zero as M (x value in Fig. 4a) approaches N (indicated as color

in Fig. 4a). In other words, when fitting high dimensional MPEA energy ($N \to \infty$) with basis with

similar but lower dimensionality ($M \to N - 1$), the fitting error for all clusters will approximate

infinitely to zero. This also indicates that the prediction of high-dimensional MPEA stability will

be much more accurate as dimensionality goes up. To validate our model with higher-dimensional

DFT-computed MPEAs, we generate an additional dataset comprising 9,362 DFT-calculated

equimolar MPEAs ranging from 6M to 10M MPEAs. This includes: (i) a BCC refractory dataset

containing 6M, 8M, and 9M MPEAs composed of Ti, V, Cr, Zr, Nb, Mo, Hf, Ta, and W; (ii) two

FCC datasets covering 6M, 8M, 9M, and 10M MPEAs, one constructed from the compositional

space of Ti, V, Cr, Mn, Fe, Co, Ni, Cu, Zn, and Al, and the other from V, Cr, Mn, Fe, Co, Ni, Cu

combined with at least one metal from Ru, Rh, Pd, Ag, Ir, Pt, and Au. The fitting errors using

lower-dimensional basis to predict on the higher-dimensional data are shown in Fig. 4b. Our results

confirm that low-dimensional MPEAs can reliably estimate the energies of higher-dimensional

systems. The same trend of MAE evolution (Fig. 4a) is observed when fitting lower-dimensional

DFT-computed SQS structures to higher dimensions (Fig. 4b), where mean absolute error (MAE)

is calculated as the average of the absolute errors between the predicted and DFT total energies. Notably, prediction accuracy improves as the dimensionality of the basis approaches that of the target system, and tends to converge at higher dimensions, with MAEs as low as 6.956 meV/atom when using 8M MPEA basis to predict 9M compositions. The predicted total energies of higher-dimensional alloys can then be used to construct the convex hull and determine the corresponding E_{hull} values, which can rapidly estimate synthesizability. When comparing with typical Hume-Rothery descriptors, such as the average and standard deviation of atomic radius and electronegativity, the relationship with formation energy is weak, with the maximum absolute Pearson correlation coefficient (|PCC|) being only 0.380, as shown in Supplementary Figure 8. This further underscores the strength of our physical model in providing both quantitative accuracy and physical interpretability. It should be noted that the model is constructed from zero-temperature total energies; it can serve as a baseline for estimating entropy-stabilization temperatures but more accurate estimation of all types of entropies will greatly enhance the accuracy of the stability prediction[75]. Our DFT fitting analysis not only supports the viability of previously reported theoretical attempts, which use binary formation energy or pairwise energy to predict promising single-phase high-dimensional alloys[20,60,76], but also explains why the reported fitting errors are much larger than what we obtained and how to improve.

We also compare the accuracy of our physical model with the state-of-the-art convolutional neural network (e.g., crystal graph convolutional neural network (CGCNN))[31]. In recent work[32], we showed that CGCNN stands out among several graph neural network models for predicting the stability of MPEAs, so we use it for this comparison. By fitting both models with the same dataset, our physical model shows similar, and in most cases, better performance compared to CGCNN (Fig. 4c), and MAEs are shown in Supplementary Table 4. For target dimensionalities greater than

five, the training data for CGCNN consists of all lower-dimensional compositions sampled within the same expanded compositional space, rather than the entire dataset of lower-dimensional systems. More importantly, our approach requires no training on GPUs or high-performance CPUs as all we need to do is to determine coefficient ε^i once the energy basis is computed, while the easiest yet effective ε^i is $\frac{1}{C_N^M}$ (the comparison with us coefficient is provided in Supplementary Figure 9). In particular, when using materials with mixed dimensionalities to predict higher-dimensional MPEAs, the prediction error can be further optimized as the cluster concentration from low-dimensional basis can match better with higher-dimensional MPEAs (detailed in Supplementary Note 4, Supplementary Table 5 and Supplementary Figure 10).

Discussion

Capabilities and limitations of synthesizability prediction

The impressive accuracy of our universal framework enables the rapid prediction of MPEA energetics and can be readily adapted to estimate synthesizability through E_{hull} values and phase diagram calculations. Although the criterion $E_{hull} < S_{ideal} \times T$ is a rough approximation, it has been widely adopted as an effective indicator for predicting stability in compositionally complex and high-entropy materials[34,77,78]. To further evaluate the capabilities and limitations of E_{hull} beyond the nine experiments shown in Fig. 2, we compile 32 additional reported equimolar MPEA compositions (Supplementary Table 6), all of which have been experimentally synthesized below 1273 K. Among these 32 compositions, 30 are predicted to be synthesizable by our DFT-based phase diagram calculations. In contrast, for the literature-reported equimolar compositions that failed to form a single phase (Supplementary Table 7), all 30 collected compositions exhibit positive $E_{hull} - S_{ideal} \times 1273K$ values. Taken together, these results support the use of the criterion $E_{hull} < S_{ideal} \times T$ as a reasonable approximation for synthesizability. This further implies that our

universal framework (Fig. 4) can be used to rapidly predict the synthesizability of a broad range of MPEAs.

The E_{hull} values and phase diagram calculations adopted in this work are certainly not perfect metric for estimating synthesizability. They may fail to predict the synthesizability and require a thorough synthesis design of some MPEAs, particularly for compounds near the synthesizability boundary (e.g., E_{hull} - $S_{ideal} \times 1273K$ being close to zero). Incorporating vibrational free energy and chemical short-range order (CSRO)[34,79-81] would undoubtedly improve accuracy, but such calculations remain computationally impractical for large-scale datasets, especially when considering hundreds of thousands of compositions across a 28-element space. It would also be valuable to account for competition with lower-dimensional disordered phases. However, this is also currently infeasible, as it would require mapping the full free energy landscape across all relevant phases and compositions, including accurate evaluations of both vibrational entropy and CSRO. Given these constraints, the approximation adopted in this study represents the most practical and computationally efficient approach for exploring the global MPEA space until now, and it is further validated by the successful synthesis of many predicted compounds[34,77,78]. Finally, it is important to note that failure to synthesize a compound after one or two attempts does not necessarily imply that the corresponding MPEA is inaccessible. For certain compositions, more deliberate synthetic design and systematic experimental efforts are required to fully assess their synthesizability.

Physical interpretations of the universal framework

The simple linear model we propose is accurate, with MAE as low as 6.956 meV/atom (Fig. 4b). The origins of the fitting errors retain full interpretability through cluster expansion theory [65,66,82,83]. Specifically, the fitting errors come from four major sources: 1) the different

contributions from cluster probability due to the mismatch of higher order cluster coefficients (detailed in Supplementary Note 3); 2) the missing of higher order cross-interactions in low-dimensional bases. For instance, there are no A-B-C-D interactions in ternary MPEAs; 3) the imperfection of using a finite cell to approximate a random limit, as SQS cannot always ensure exact random cluster probability; 4) the possibility of DFT errors in relaxing MPEAs. However, as implied by our fitting errors up to quinary MPEAs, the model is already powerful and accurate despite these intrinsic sources of errors (Fig. 4).

Moreover, the expansion and parameterization of Equation (2) may not be ideal for predicting MPEAs with CSRO, which will make cluster probability deviate from the random limit. However, given that CSRO signal is not very strong in MPEAs and will become weaker, in general, when MPEAs go to much higher dimension [34,80,84-86]. It should, in general, be reliable to estimate the energy of high-dimensional MPEAs with our proposed model, even with the existence of CSRO. When needed, a more complicated basis can be developed with the formulism approximating a real cluster expansion. Several examples and how they behave are presented in Supplementary Note 4 and Supplementary Figure 10.

The fitting error of our model can be physically interpreted as the generalized mixing enthalpy to form a high-dimensional MPEA through equimolar mixing of lower-dimensional MPEAs. We observe that the fitting error generally decreases when modelling MPEAs of N dimensions as the basis dimensionality (M) approaches N ($M \rightarrow N - 1$) (Fig. 4). This suggests that the driving force for high-dimensional MPEAs to decompose from N-dimensions to N-1-dimensions is typically very small. This reveals an unprecedented feature of the thermodynamics of ultra-high-entropy alloys: as the dimensionality of MPEAs increases, the decomposition energy to lower-dimensional MPEAs diminishes. This discovery could potentially lead to numerous

synthetic innovations in MPEAs, as the weaker thermodynamic driving force for the decomposition of ultra-high-entropy alloys allows for a variety of kinetically favorable processes to be employed in the synthesis of MPEAs. In the current validation dataset, we include exclusively equimolar MPEA compositions, which lie at the center of the compositional space and exhibit the strongest high-entropy effect. Non-equimolar compositions are not included in our dataset primarily due to the vastness of their compositional space, which lacks the constraint of equal atomic fractions and is therefore significantly larger and more complex to sample systematically. Nevertheless, our physical model is, in principle, applicable to non-equimolar compositions, but further exploration of the linear combination coefficients will be needed.

Building on this thermodynamic interpretation, our physical linear model predicts the energy and hence stability of high-dimensional MPEAs using a weighted linear average of the lower-dimensional MPEA as basis. Fitting such model eliminates the need for training on GPUs or high-performance CPUs. The determination of coefficient is through solving a set of linear equations or as simple as setting a weighting factor $\varepsilon^i = \frac{1}{C_N^M}$. For specific subspace of MPEA of interest, there is no need to develop a comprehensive training data, instead, one can simply use lower-entropy equimolar basis at a given dimension, e.g., ternary or quaternary MPEAs. While inspired by the cluster expansion formalism[65,82,87], our framework does not involve conventional cluster expansion fitting, which would require millions to billions of DFT calculations across a 28-element space. Instead, we estimate the energy of an N-component equimolar alloy as a linear combination of lower-dimensional subspaces. Earlier work has demonstrated that binary interaction energetics provide guidance for identifying single-phase candidates in compositionally complex alloys[20]. Building upon this physical foundation, we demonstrate that Cluster Expansion concepts can be adapted to justify a more data-efficient and physically interpretable model for

predicting MPEA stability. Moreover, the application of our model does not need further relaxation using Hamiltonian such as machine learning force field, which are required by the state-of-the-art foundational models[88]. We thus believe this discovery will facilitate the rapid exploration of unexplored MPEA space.

In this study, we employ high-throughput computation to elucidate stability rules for MPEAs across compositions and dimensions. We have generated a dataset comprised of binary to quinary MPEAs constructed from 28 metal elements. Nine non-reported noble-metal-containing (six quaternary and three quinary) MPEAs (with $T_{stable} < 1273$ K) were successfully synthesized to validate the reliability of our computational evaluation. More importantly, we have revealed that a linear physical model can be used to estimate the stability of MPEAs and that this model offers accuracy comparable to that of the state-of-the-art deep learning models. We also reveal that the prediction of ultra-high entropy MPEAs may be less challenging than previously thought, as the mixing enthalpy of forming higher-dimensional MPEAs from lower-dimensional MPEAs decreases as the dimensionality goes up.

Methods

Multi-principal element alloys (MPEA) structures and phase stability

All disordered MPEAs investigated in this work were generated using the special quasi-random structure (SQS) approach.[73] The pymatgen package (v2024.5.1) [89] and ATAT codes [90] were used to generate the SQS structures. Three typical structures, BCC, FCC, and HCP, were generated for every composition.[3] A supercell consisting of 96 atoms was used for all binary, ternary and quaternary structures, a supercell consisting of 120 atoms was used for quinary structures. BCC and FCC systems with six or eight metals were modeled using 120- or 144-atom supercells; 9-metal systems used 144-atom supercells, and 10-metal FCC systems used 180-atom supercells. We have generated a complete dataset for MPEAs consisting of two, three, or four

metal elements selected from 28 elements[3], and a customized dataset for high-entropy alloys with 5-10 metals. The structures of competing phases were extracted from the Materials project [36] and OQMD datasets [37]. We used pymatgen to construct the phase diagram [33,91] and calculate the energy above hull (denoted as E_{hull}, in units of meV/atom) for all MPEAs.

Electronic structure calculations

All electronic structure calculations were performed using the Vienna Ab-initio Simulation Package (VASP, version 6.2.1) [92-94] with PBE functionals [95] and PAW pseudopotentials [96,97]. A reciprocal space discretization of 25 k-points per Å^{-1} was used to sample the Brillouin zone.[98] The kinetic energy cutoff was 520 eV. The Methfessel-Paxton scheme was used to smooth the partial occupancies for each orbital [99], with a smearing width of 0.2 eV. The convergence criterion for the self-consistent field (SCF) step was 10^{-5} eV/atom. Geometric optimizations were executed until the force on each atom was less than 0.05 eV.

Experimental Materials.

Poly(ethylene oxide)-*b*-poly(2-vinyl pyridine) (PEO-*b*-P2VP, M_n = 2.8-b-1.5 kg/mol, M_w/M_n = 1.11) and polystyrene (M_n = 10 kg/mol, M_w/M_n = 1.09) were purchased from Polymer Source, Inc. All other chemicals were purchased from Sigma-Aldrich and used as received, including manganese(II) nitrate tetrahydrate ($Mn(NO_3)_2 \cdot 4H_2O$, 99.9%), iron(III) nitrate nonahydrate ($Fe(NO_3)_3 \cdot 9H_2O$, 99.999%), cobalt(II) nitrate hexahydrate ($Co(NO_3)_2 \cdot 6H_2O$, 99.999%), nickel(II) nitrate hexahydrate ($Ni(NO_3)_2 \cdot 6H_2O$, 99.999%), copper(II) nitrate hemi(pentahydrate), ($Cu(NO_3)_2 \cdot 2.5H_2O$, ≥99.99%), palladium(II) nitrate dihydrate ($Pd(NO_3)_2 \cdot 2H_2O$, ~40% Pd basis), chloroplatinic acid hydrate ($H_2PtCl_6 \cdot xH_2O$, ≥99.9%), gold(III) chloride trihydrate ($HAuCl_4 \cdot 3H_2O$, ≥99.9%), iridium(III) chloride hydrate ($IrCl_3 \cdot xH_2O$, 99.9%), ruthenium(III) chloride ($RuCl_3$, 99.99%), rhodium(III) chloride hydrate ($RhCl_3 \cdot xH_2O$, ≥99.9%),

hexamethyldisilazane (HMDS), toluene, and hexane. Pen arrays (type-M, without gold coating) used for dip-pen nanolithography (DPN) were purchased from Advanced Creative Solutions Technology, Inc. Silicon nitride Transmission Electron Microscopy (TEM) window grids (100 nm with 0.1 x 0.1mm windows) and carbon films (15 nm to 25 nm) coated molybdenum TEM grids were purchased from Ted Pella, Inc.

Preparation of polymer solutions.

Polymer ink solutions were prepared by dissolving PEO-*b*-P2VP and various metal salts in deionized water, with a polymer concentration of 5 mg/mL and total metal salt concentrations of 4.0 mM. The molar ratio of different metal precursors was controlled to be equal. The pHs of the ink solutions were adjusted between 3-4 using HNO_3, followed by overnight stirring to ensure complete dissolution before use. [39]

Multimetallic nanoparticle (NP) synthesis.

Scanning probe block copolymer lithography (SPBCL) technology was used to prepare multimetallic NPs. In a typical experiment, a pen array was dip-coated with the as-prepared block copolymer ink and air dried at room temperature. The pen array was then loaded into a modified atomic force microscope (AFM) instrument (XE-150; Park Systems) in a chamber with humidity at 80%. TEM grids were first washed with isopropanol and dried under a stream of N_2, then rendered hydrophobic by either vapor-coating with HMDS for 12 hours in a desiccator or spin-coating with a 5% (w/v) polystyrene solution in toluene at 2,500 rpm, followed by baking at 110 °C for 2 minutes on a hot plate. The modified TEM grids were used as the patterning substrates and transferred into a tube furnace after patterning. The thermal treatment conditions were as follows: ramp to 150 °C under H_2 in 10 min, hold at 150 °C for 10 h, ramp to 500 °C in 1 h, hold at 500 °C for 10 h, ramp to 1000 °C in 1 h, hold at 1000 °C for 2 h, and quench to room temperature.

Characterization

Scanning transmission electron microscopy (STEM) images were taken with a Hitachi HD-2300 STEM at an acceleration voltage of 200 kV. The composition of various NPs was determined with the dual energy-dispersive X-ray spectroscopy (EDS) detectors on the same instrument. Elemental mapping and composition quantification were conducted using the Lα peaks for Au, Pt, Pd, Ir, Rh, and Ru, and the Kα peaks for Mn, Fe, Co, Ni, and Cu from the EDS spectra. Atomic compositions of the NPs were calculated based on EDS spectral analysis with the Cliff-Lorimer correction method, with an inherent error of less than 5% due to X-ray absorption and fluorescence. Background subtraction in the EDS maps was performed using Thermo Scientific NSS software.

Data availability:

All data for reproducing this work have been included in manuscript and supplementary information. Source data is provided with this paper. All data generated or analyzed in this study are provided in the Source Data file included with this manuscript. There are no restrictions on data access.

References

1. George, E. P., Raabe, D. & Ritchie, R. O. High-entropy alloys. *Nat Rev Mater* **4**, 515-534 (2019).
2. Senkov, O. N., Miller, J. D., Miracle, D. B. & Woodward, C. Accelerated exploration of multi-principal element alloys with solid solution phases. *Nature Communications* **6**, 6529 (2015).
3. Wang, L. & Ouyang, B. Phase Selection Rules of Multi-Principal Element Alloys. *Advanced Materials* **36**, 2307860 (2024).
4. Miracle, D. B. & Senkov, O. N. A critical review of high entropy alloys and related concepts. *Acta Materialia* **122**, 448-511 (2017).
5. Hsu, W.-L., Tsai, C.-W., Yeh, A.-C. & Yeh, J.-W. Clarifying the four core effects of high-entropy materials. *Nature Reviews Chemistry*, 1-15 (2024).
6. Ye, Z. et al. Using Surface Composition and Energy to Control the Formation of Either Tetrahexahedral or Hexoctahedral High-Index Facet Nanostructures. *Journal of the American Chemical Society* **146**, 13519-13526 (2024).
7. Ye, Z. et al. A data-driven approach for the guided regulation of exposed facets in nanoparticles. *Nature Synthesis* **3**, 922-929 (2024).

8. Dey, G. R. et al. Colloidal Nanoparticles of High Entropy Materials: Capabilities, Challenges, and Opportunities in Synthesis and Characterization. *ACS Nanoscience Au* **4**, 3-20 (2024).

9. Veglak, J. M., Tsai, A., Soliman, S. S., Dey, G. R. & Schaak, R. E. Disentangling Competitive and Synergistic Chemical Reactivities During the Seeded Growth of High-Entropy Alloys on High-Entropy Metal Sulfide Nanoparticles. *Journal of the American Chemical Society* **146**, 19521-19536 (2024).

10. Yang, C. et al. Overcoming immiscibility toward bimetallic catalyst library. *Science Advances* **6**, eaaz6844 (2020).

11. Yao, Y. et al. High-entropy nanoparticles: Synthesis-structure-property relationships and data-driven discovery. *Science* **376**, eabn3103

12. Cui, M. et al. Multi-principal elemental intermetallic nanoparticles synthesized via a disorder-to-order transition. *Science Advances* **8**, eabm4322

13. Birbilis, N., Choudhary, S., Scully, J. R. & Taheri, M. L. A perspective on corrosion of multi-principal element alloys. *npj Materials Degradation* **5**, 14 (2021).

14. Senkov, O. N., Miller, J. D., Miracle, D. B. & Woodward, C. Accelerated exploration of multi-principal element alloys for structural applications. *Calphad* **50**, 32-48 (2015).

15. Chen, Y. et al. A Focused Review on Engineering Application of Multi-Principal Element Alloy. *Frontiers in Materials* **8** (2022).

16. Yao, Y. et al. Computationally aided, entropy-driven synthesis of highly efficient and durable multi-elemental alloy catalysts. *Science Advances* **6**, eaaz0510

17. Sun, Y. & Dai, S. High-entropy materials for catalysis: A new frontier. *Science advances* **7**, eabg1600 (2021).

18. Bolar, S., Ito, Y. & Fujita, T. Future Prospects of High-Entropy Alloys as Next-Generation Industrial Electrode Materials. *Chemical Science* (2024).

19. Mao, X., Chen, Q. & Granick, S. Entropy favours open colloidal lattices. *Nature Materials* **12**, 217-222 (2013).

20. Troparevsky, M. C., Morris, J. R., Kent, P. R. C., Lupini, A. R. & Stocks, G. M. Criteria for Predicting the Formation of Single-Phase High-Entropy Alloys. *Physical Review X* **5**, 011041 (2015).

21. Chen, Z. & Yang, Y. Data-driven design of eutectic high entropy alloys. *Journal of Materials Informatics* **3**, 10 (2023).

22. Liu, X. et al. Machine learning-based glass formation prediction in multicomponent alloys. *Acta Materialia* **201**, 182-190 (2020).

23. He, Q. F., Ding, Z. Y., Ye, Y. F. & Yang, Y. Design of High-Entropy Alloy: A Perspective from Nonideal Mixing. *JOM* **69**, 2092-2098 (2017).

24. Yin, J., Pei, Z. & Gao, M. C. Neural network-based order parameter for phase transitions and its applications in high-entropy alloys. *Nature Computational Science* **1**, 686-693 (2021).

25. Pei, Z., Yin, J., Hawk, J. A., Alman, D. E. & Gao, M. C. Machine-learning informed prediction of high-entropy solid solution formation: Beyond the Hume-Rothery rules. *npj Computational Materials* **6**, 50 (2020).

26. Feng, R. et al. Phase stability and transformation in a light-weight high-entropy alloy. *Acta Materialia* **146**, 280-293 (2018).

27. Brown, P. & Zhuang, H. Quantum machine-learning phase prediction of high-entropy alloys. *Materials Today* **63**, 18-31 (2023).

28. Rittiruam, M. et al. High-throughput materials screening algorithm based on first-principles density functional theory and artificial neural network for high-entropy alloys. *Scientific Reports* **12**, 16653 (2022).

29. Sarker, P. et al. High-entropy high-hardness metal carbides discovered by entropy descriptors. *Nature communications* **9**, 4980 (2018).

30. Eckert, H. & Curtarolo, S. A formula to predict the synthesizability of high-entropy materials. *Nature* (2024).

31. Xie, T. & Grossman, J. C. Crystal Graph Convolutional Neural Networks for an Accurate and Interpretable Prediction of Material Properties. *Physical Review Letters* **120**, 145301 (2018).

32. Wang, L., He, T. & Ouyang, B. *The Impact of Domain Knowledge on Universal Machine Learning Models* (2024)https://doi.org/10.26434/chemrxiv-2024-fmq8p.

33. Ong, S. P., Wang, L., Kang, B. & Ceder, G. Li−Fe−P−O2 Phase Diagram from First Principles Calculations. *Chemistry of Materials* **20**, 1798-1807 (2008).

34. Lun, Z. et al. Cation-disordered rocksalt-type high-entropy cathodes for Li-ion batteries. *Nature Materials* **20**, 214-221 (2021).

35. Ouyang, B. et al. Synthetic accessibility and stability rules of NASICONs. *Nature Communications* **12**, 5752 (2021).

36. Jain, A. et al. Commentary: The Materials Project: A materials genome approach to accelerating materials innovation. *APL Materials* **1**, 011002 (2013).

37. Saal, J. E., Kirklin, S., Aykol, M., Meredig, B. & Wolverton, C. Materials Design and Discovery with High-Throughput Density Functional Theory: The Open Quantum Materials Database (OQMD). *JOM* **65**, 1501-1509 (2013).

38. Kirklin, S. et al. The Open Quantum Materials Database (OQMD): assessing the accuracy of DFT formation energies. *npj Computational Materials* **1**, 15010 (2015).

39. Chen, P.-C. et al. Interface and heterostructure design in polyelemental nanoparticles. *Science* **363**, 959-964 (2019).

40. Chen, P.-C. et al. Polyelemental nanoparticle libraries. *Science* **352**, 1565-1569 (2016).

41. Tsao, T.-K., Sheikh, S. & Murakami, H. Development of platinum-group-metals-containing high entropy alloys with outstanding thermal capability and hot hardness. *Applied Physics Letters* **119**, 191901 (2021).

42. Shen, B. et al. Crystal structure engineering in multimetallic high-index facet nanocatalysts. *Proceedings of the National Academy of Sciences* **118**, e2105722118 (2021).

43. Sreeramagiri, P. & Balasubramanian, G. Directed Energy Deposition of Multi-Principal Element Alloys. *Frontiers in Materials* **9** (2022).

44. Borg, C. K. H. et al. Expanded dataset of mechanical properties and observed phases of multi-principal element alloys. *Scientific Data* **7**, 430 (2020).

45. Coury, F. G., Zepon, G. & Bolfarini, C. Multi-principal element alloys from the CrCoNi family: outlook and perspectives. *Journal of Materials Research and Technology* **15**, 3461-3480 (2021).

46. Huang, L. et al. Multimetallic High-Index Faceted Heterostructured Nanoparticles. *Journal of the American Chemical Society* **142**, 4570-4575 (2020).

47. Qi, J., Cheung, A. M. & Poon, S. J. High Entropy Alloys Mined From Binary Phase Diagrams. *Scientific Reports* **9**, 15501 (2019).

48. Li, M. et al. High-entropy alloy electrocatalysts go to (sub-)nanoscale. *Science Advances* **10**, eadn2877 (2024).

49.   Sun, W., Kitchaev, D. A., Kramer, D. & Ceder, G. Non-equilibrium crystallization pathways of manganese oxides in aqueous solution. *Nature Communications* **10**, 573 (2019).
50.   Chen, B.-R. et al. Understanding crystallization pathways leading to manganese oxide polymorph formation. *Nature Communications* **9**, 2553 (2018).
51.   Piner, R. D., Zhu, J., Xu, F., Hong, S. & Mirkin, C. A. "Dip-Pen" Nanolithography. *Science* **283**, 661-663 (1999).
52.   Huo, F. et al. Polymer Pen Lithography. *Science* **321**, 1658-1660 (2008).
53.   Chai, J. et al. Scanning probe block copolymer lithography. *Proceedings of the National Academy of Sciences* **107**, 20202-20206 (2010).
54.   Shen, B. et al. Morphology Engineering in Multicomponent Hollow Metal Chalcogenide Nanoparticles. *ACS Nano* **17**, 4642-4649 (2023).
55.   Shen, B. et al. Synthesis of Metal-Capped Semiconductor Nanowires from Heterodimer Nanoparticle Catalysts. *Journal of the American Chemical Society* **142**, 18324-18329 (2020).
56.   Smith, P. T., Wahl, C. B., Orbeck, J. K. H. & Mirkin, C. A. Megalibraries: Supercharged acceleration of materials discovery. *MRS Bulletin* **48**, 1172-1183 (2023).
57.   Lai, M., Shin, D., Jibril, L. & Mirkin, C. A. Combinatorial Synthesis and Screening of Mixed Halide Perovskite Megalibraries. *Journal of the American Chemical Society* **144**, 13823-13830 (2022).
58.   Hume-Rothery, W. Researches on the nature, properties, and conditions of formation of intermetallic compounds, with special reference to certain compounds of tin. (1926).
59.   Pickering, E. J., Muñoz-Moreno, R., Stone, H. J. & Jones, N. G. Precipitation in the equiatomic high-entropy alloy CrMnFeCoNi. *Scripta Materialia* **113**, 106-109 (2016).
60.   Chen, W. et al. A map of single-phase high-entropy alloys. *Nature Communications* **14**, 2856 (2023).
61.   Ye, Y. F., Wang, Q., Lu, J., Liu, C. T. & Yang, Y. High-entropy alloy: challenges and prospects. *Materials Today* **19**, 349-362 (2016).
62.   Cantor, B. Multicomponent high-entropy Cantor alloys. *Progress in Materials Science* **120**, 100754 (2021).
63.   Magyari-Köpe, B., Vitos, L. & Grimvall, G. Anomalous behavior of lattice parameters and elastic constants in hcp Ag− Zn alloys. *Physical Review B* **70**, 052102 (2004).
64.   Liu, S., Liu, B., Gong, C. & Li, Z. A nanoporous Cu-Ag thin film at the Cu-Ag-Zn alloy surface by spontaneous dissolution of Zn and Cu in different degrees as a highly sensitive non-enzymatic glucose sensor. *Electrochimica Acta* **320**, 134599 (2019).
65.   Barroso-Luque, L. et al. Cluster expansions of multicomponent ionic materials: Formalism and methodology. *Physical Review B* **106**, 144202 (2022).
66.   Sanchez, J. M., Ducastelle, F. & Gratias, D. Generalized cluster description of multicomponent systems. *Physica A: Statistical Mechanics and its Applications* **128**, 334-350 (1984).
67.   Sanchez, J. M. Cluster expansions and the configurational energy of alloys. *Physical Review B* **48**, 14013-14015 (1993).
68.   Tepesch, P. D., Garbulsky, G. D. & Ceder, G. Model for Configurational Thermodynamics in Ionic Systems. *Physical Review Letters* **74**, 2272-2275 (1995).

69. Asta, M., Foiles, S. M. & Quong, A. A. First-principles calculations of bulk and interfacial thermodynamic properties for fcc-based Al-Sc alloys. *Physical Review B* **57**, 11265-11275 (1998).

70. Nguyen, A. H., Rosenbrock, C. W., Reese, C. S. & Hart, G. L. W. Robustness of the cluster expansion: Assessing the roles of relaxation and numerical error. *Physical Review B* **96**, 014107 (2017).

71. Levy, O., Hart, G. L. W. & Curtarolo, S. Uncovering Compounds by Synergy of Cluster Expansion and High-Throughput Methods. *Journal of the American Chemical Society* **132**, 4830-4833 (2010).

72. Sanchez, J. M., Ducastelle, F. & Gratias, D. Generalized cluster description of multicomponent systems. *Physica A: Statistical Mechanics and its Applications* **128**, 334-350 (1984).

73. Zunger, A., Wei, S. H., Ferreira, L. G. & Bernard, J. E. Special quasirandom structures. *Physical Review Letters* **65**, 353-356 (1990).

74. van de Walle, A. et al. Efficient stochastic generation of special quasirandom structures. *Calphad* **42**, 13-18 (2013).

75. Esters, M. et al. Settling the matter of the role of vibrations in the stability of high-entropy carbides. *Nature Communications* **12**, 5747 (2021).

76. Zhang, Z., Li, M., Cavin, J., Flores, K. & Mishra, R. A Fast and Robust Method for Predicting the Phase Stability of Refractory Complex Concentrated Alloys using Pairwise Mixing Enthalpy. *Acta Materialia* **241**, 118389 (2022).

77. Sun, W. et al. The thermodynamic scale of inorganic crystalline metastability. *Science Advances* **2**, e1600225 (2016).

78. Wang, L. et al. Elemental Stability Rules for High Entropy Disordered Rocksalt Type Li-Ion Battery Positive Electrodes. *Advanced Energy Materials* **15**, 2404982 (2025).

79. Walsh, F., Zhang, M., Ritchie, R. O., Minor, A. M. & Asta, M. Extra electron reflections in concentrated alloys do not necessitate short-range order. *Nature Materials* **22**, 926-929 (2023).

80. Zhang, R. et al. Short-range order and its impact on the CrCoNi medium-entropy alloy. *Nature* **581**, 283-287 (2020).

81. Yin, B., Yoshida, S., Tsuji, N. & Curtin, W. A. Yield strength and misfit volumes of NiCoCr and implications for short-range-order. *Nature Communications* **11**, 2507 (2020).

82. Sanchez, J. M. & de Fontaine, D. The fcc Ising model in the cluster variation approximation. *Physical Review B* **17**, 2926-2936 (1978).

83. Sanchez, J. M. & de Fontaine, D. in *Industrial Chemistry Library* Vol. 2 (eds Michael O'Keeffe & Alexandra Navrotsky) 117-132 (Elsevier, 1981).

84. Zhang, R. et al. Direct imaging of short-range order and its impact on deformation in Ti-6Al. *Science Advances* **5**, eaax2799

85. Seol, J. B. et al. Mechanically derived short-range order and its impact on the multi-principal-element alloys. *Nature Communications* **13**, 6766 (2022).

86. Ferrari, A., Körmann, F., Asta, M. & Neugebauer, J. Simulating short-range order in compositionally complex materials. *Nature Computational Science* **3**, 221-229 (2023).

87. Ouyang, B. et al. Effect of Fluorination on Lithium Transport and Short-Range Order in Disordered-Rocksalt-Type Lithium-Ion Battery Cathodes. *Advanced Energy Materials* **10**, 1903240 (2020).

88. Riebesell, J. et al. Matbench Discovery--A framework to evaluate machine learning crystal stability predictions. *arXiv preprint arXiv:2308.14920* (2023).

89. Ong, S. P. et al. Python Materials Genomics (pymatgen): A robust, open-source python library for materials analysis. *Computational Materials Science* **68**, 314-319 (2013).

90. van de Walle, A., Asta, M. & Ceder, G. The alloy theoretic automated toolkit: A user guide. *Calphad* **26**, 539-553 (2002).

91. Ong, S. P., Jain, A., Hautier, G., Kang, B. & Ceder, G. Thermal stabilities of delithiated olivine MPO4 (M=Fe, Mn) cathodes investigated using first principles calculations. *Electrochemistry Communications* **12**, 427-430 (2010).

92. Kresse, G. & Furthmüller, J. Efficiency of ab-initio total energy calculations for metals and semiconductors using a plane-wave basis set. *Computational materials science* **6**, 15-50 (1996).

93. Kresse, G. & Hafner, J. Ab initio molecular-dynamics simulation of the liquid-metal–amorphous-semiconductor transition in germanium. *Physical Review B* **49**, 14251 (1994).

94. Kresse, G. & Hafner, J. Ab initio molecular dynamics for liquid metals. *Physical review B* **47**, 558 (1993).

95. Perdew, J. P., Burke, K. & Ernzerhof, M. Generalized gradient approximation made simple. *Physical review letters* **77**, 3865 (1996).

96. Blöchl, P. E. Projector augmented-wave method. *Physical review B* **50**, 17953 (1994).

97. Kresse, G. & Joubert, D. From ultrasoft pseudopotentials to the projector augmented-wave method. *Physical review b* **59**, 1758 (1999).

98. Monkhorst, H. J. & Pack, J. D. Special points for Brillouin-zone integrations. *Physical Review B* **13**, 5188-5192 (1976).

99. Methfessel, M. & Paxton, A. T. High-precision sampling for Brillouin-zone integration in metals. *Physical Review B* **40**, 3616-3621 (1989).

Acknowledgments

Author Contributions Statement:

B.O. supervised and planned all aspects of the research.; B.O., L.W. designed the computations and generated all computational results; B.O., L.W., and Z.H. analyzed the data and generated all figures; B.S., Z.Y. did chemical synthesis and analysis; L. W., B. S., Z. Y., Y. Z., C. M., and B. O. contributed to the writing.

Corresponding author: Correspondence to Bin Ouyang (bouyang@fsu.edu)

Competing interests Statement:

The authors declare that they have no competing interests.

Figure Captions:

Fig. 1. Chemical space and data distribution of the MPEA dataset. a, The bottom left triangle represents the room temperature phases as elemental metal of selected metal, Mn and Sn marked as "other" because the room temperature phases are none of the three phases (BCC/FCC/HCP). The top-right triangle distinguishes each metal as either a noble or a non-noble metal; **b**, Scatter plot of formation energy (E_{form}) and energy above hull (E_{hull}) for all 4M MPEAs that can be entropically stabilized below 2000 K (the stabilization temperature is calculated from E_{hull}/S_{ideal}. Here, S_{ideal} is the ideal mixing entropy, defined as $S_{ideal} = k_B ln(n_M)$ with k_B as the Boltzmann constant and n_M as the number of metal elements in MPEA). Blue and red represent low and high temperatures, respectively. The solid black line represents the line $E_{form} = E_{hull}$. Three dashed lines represent the maximum E_{hull} values of 4M MPEAs that can be stabilized at 500 K, 1000 K, and 2000 K, respectively, assuming ideal mixing entropy.

Fig. 2. Previously reported noble metal-containing MPEAs and non-reported MPEAs discovered in this work. a, Number of papers published on noble-metal-containing MPEAs from 2000 to 2024 (Counts are derived from papers listed in the Supplementary References). **b**, Histogram of the energy above hull of the noble-metal-containing 3-5M MPEAs investigated in this work. The dashed lines represent where the entropy-stabilization temperature is less than 1273 K. **c**, STEM images and EDX elemental mappings of six synthesized noble-metal-containing 4M MPEAs with different compositions. **d**, STEM images and EDX elemental mappings of three synthesized noble-metal-containing 5M MPEAs with different compositions. Scale bars = 10 nm.

Fig. 3. Chord diagrams showing the pair-wise elemental stability of MPEAs. a, Pairs between all metals. b, Pairs between noble-noble metals. c, Pairs between non-noble metals. (d-k) Pair-wise connection for each noble metal (the same color is shown in a). Thickness is set in proportion to the probability of finding MPEA with given two metals with stabilization temperatures below 1273 K. Note that all chord diagrams from A to K have the same order of elements so that the small font size in D-K can be seen using A as a reference.

Fig. 4. Performance of our predictive model. a, The theoretically derived mean absolute error (MAE) of predicting energy contribution from selective cluster 4M-10M MPEA using 2M-9M MPEA as basis. J_0 is used to represent the unit of energy, with the physical meaning being the energy contribution of certain cluster, e.g., J_{ii}, J_{ij}, J_{ijk} respectively. **b**, The MAE for using DFT-computed total energy of 2M-9M MPEA to predict 4M-10M MPEAs as a contrast to the theoretical derivation. **c**, The comparison between our physical model with a crystal graph convolutional neural network (CGCNN). Each bar represents a single value, not a statistical distribution.

Editorial Summary

This work introduces a simple and interpretable model that predicts the stability of multi-principal element alloys. By using energies from lower-dimensional systems, the model achieves high accuracy and is validated by experiments.

Peer Review Information: *Nature Communications* thanks the anonymous, reviewer(s) for their contribution to the peer review of this work. A peer review file is available.